VELOCITY, POTENTIAL, AND TEMPERATURE DISTRIBUTIONS IN MOLTEN METALS DURING ELECTROMAGNETIC STIRRING. PART II: NUMERICAL SIMULATIONS

Amnon J. Meir
Department of Mathematics, 218 Parker Hall
Auburn University, Alabama 36849-5310, USA
Phone: (334) 844-6580 Fax: (334) 844-6555

Paul G. Schmidt
Department of Mathematics, 218 Parker Hall
Auburn University, Alabama 36849-5310, USA
Phone: (334) 844-6579 Fax: (334) 844-6555

Sayavur I. Bakhtiyarov
Space Power Institute, 231 Leach Science Center
Auburn University, Alabama 36849-5320, USA
Phone: (334) 844-6198 Fax: (334) 844-5900

Ruel A. Overfelt
Department of Mechanical Engineering, 201 Ross Hall
Auburn University, Alabama 36849-5341, USA
Phone: (334) 844-5940 Fax: (334) 844-3307

ABSTRACT

We describe a novel approach to the mathematical modeling and computational simulation of fully three-dimensional, electromagnetically and thermally driven liquid-metal flow. The phenomenon is governed by the Navier-Stokes equations, Maxwell's equations, Ohm's law, and the heat equation, all nonlinearly coupled via Lorentz and electromotive forces, buoyancy forces, and convective and dissipative heat transfer. Employing the electric current density rather than the magnetic field as the primary electromagnetic variable, it is possible to avoid artificial or highly idealized boundary conditions for electric and magnetic fields and to account exactly for the electromagnetic interaction of the fluid with the surrounding media. A finite-element method based on this approach was used to simulate the flow of a metallic melt in a cylindrical container, rotating steadily in a uniform magnetic field perpendicular to the cylinder axis. Velocity, pressure, current, and potential distributions were computed and compared to theoretical predictions.

INTRODUCTION

Electromagnetic stirring of metallic melts is widely used in the metals processing industry, mostly in order to improve the solidification structure of casting products. The stirring is brought about by Lorentz forces, resulting from the interaction of an applied magnetic field with eddy currents in the melt; those currents are induced by relative motion between the melt and magnetic field. A standard technique is to generate a rotating magnetic field in an inductor surrounding a stationary column of molten metal; alternatively, the metal may be rotated in a stationary magnetic field. In any event, qualitative and quantitative understanding of the ensuing flow patterns is of critical importance in achieving optimal stirring conditions. Efficient and accurate experimental and computational techniques are needed to measure and to predict velocity, current, and temperature distributions in the melt. Despite considerable research efforts over the past three decades, the methodology is still in need of development. This is due to the complexity of the underlying flow phenomena, which are, in general, fully three-dimensional, highly nonlinear, and characterized by the interaction of multiple physical effects (involving hydrodynamics, electrodynamics, and thermodynamics).

Beginning with Moffatt (1965), numerous researchers have studied the electromagnetic stirring of round strands of liquid metal by the rotating-field method; see, for example, Spitzer et al. (1986), Davidson and Hunt (1987), and Saluja et al. (1990). Mathematically, these investigations are based on the assumption of a circular-cylindrical geometry and the numerical solution or asymptotic analysis of the stationary Navier-Stokes equations, usually in conjunction with a suitable turbulence model, under a known distribution of time-averaged Lorentz forces. The latter are determined from an asymptotic solution of the magnetic induction equation under appropriate boundary conditions for the magnetic field. Many simplifying assumptions are made, and the analysis depends heavily on the axisymmetry of the problem (none of the relevant quantities depend on the angular variable). Heat transfer effects due to temperature fluctuations in the melt are neglected. Nevertheless, these investigations have provided valuable insights into the structure of the flow field in a rotationally stirred column of liquid metal. The main finding is that

in addition to a purely azimuthal primary flow in the region surrounded by the inductor, there is a strong secondary flow with radial and axial components, which reaches far beyond the stirrer region. For more experimentally rooted studies of rotational stirring, involving different geometries and accounting for heat transfer effects, see, for example, Meyer et al. (1984), Vivès and Ricou (1985), and most recently, Cho et al. (1999).

The interaction of *stationary* magnetic fields with moving metallic melts has been exploited, for example, in connection with the damping of buoyancy-driven flows during solidification (Prescott and Incropera, 1993), but appears to be largely untested in the context of electromagnetic stirring. Although based on the same principle, the effect of rotating the melt in a stationary, transverse magnetic field is quite different from that of traditional rotational stirring. In particular, the resulting flow field cannot be expected to be rotationally symmetric; in fact, the induced flow will be symmetric with respect to the axis of the magnetic field rather than the axis of rotation (see Figure 3 and the discussion at the end of Section 3). As a consequence, the flow is fully three-dimensional, even in the simplest experimental configuration (cylindrical crucible of circular cross-section, uniform magnetic field perpendicular to the cylinder axis, uniform temperature distribution). Another difference, as compared to traditional rotational stirring, is the absence of a skin effect. In the presence of a rotating magnetic field, two distinct magnetic Reynolds numbers are of relevance, one based on the characteristic velocity of the melt, the other on the angular frequency of the rotating field; the latter is inversely proportional to the square of the skin depth. All the above-referenced papers on rotational stirring of round strands invoke varying assumptions on the relative size of the two magnetic Reynolds numbers, leading to low-frequency and high-frequency approximations, respectively. For a rotating crucible in a stationary magnetic field, these considerations are irrelevant.

The objective of this paper is to present a general approach to the modeling and simulation of liquid-metal flows, as applied to the flow of a metallic melt in a circular-cylindrical crucible, rotating steadily in a uniform magnetic field perpendicular to the cylinder axis (the axis of rotation). A corresponding experimental apparatus and measurement technique are described in a companion paper (Bakhtiyarov et al., 1999), elsewhere in these proceedings. The present analysis differs from earlier work not only in that it addresses a nontraditional stirring mechanism, but more importantly, in that it is based on the direct numerical simulation of the full, nonlinear, three-dimensional, electromagnetically and thermally coupled flow problem. The mathematical foundation is a mixed variational formulation and finite-element discretization of the (stationary) Navier-Stokes equations, Maxwell's equations, Ohm's law, and the heat equation, coupled via Lorentz and electromotive forces, buoyancy forces, and convective and dissipative heat transfer. One key feature is the use of the electric current density (rather than the magnetic field) as the primary electromagnetic variable; this renders artificial or highly idealized electromagnetic boundary conditions obsolete. We refer to Meir and Schmidt (1999b) for mathematical details and to Meir and Schmidt (1998, 1999a) for prior applications to electromagnetically driven flows.

Section 1 is concerned with the mathematical model, Section 2 with discretization and implementation issues. In Section 3 we describe preliminary computational experiments, thus far limited to the laminar flow regime and not accounting for temperature fluctuations. Implementation of a turbulence model and a heat transfer model is the subject of ongoing work.

1. MATHEMATICAL MODEL

We are concerned with the steady flow of a viscous, incompressible, electrically and thermally conducting fluid, confined to a cylindrical crucible, in the presence of gravity, an applied magnetic field, and a radiative heat source; see Bakhtiyarov et al. (1999) for a detailed description of the experimental apparatus. We assume the presence of a lid on top of the fluid, thus avoiding the complication of a free surface; also neglected is the thickness of the crucible walls. The problem is governed by balance equations for momentum, mass, and energy, along with Maxwell's equations and Ohm's law; see Hughes and Young (1966) for the physical background.

The momentum balance is given by the stationary Navier-Stokes equations,

$$-\eta\nabla^2\mathbf{V} + \rho(\mathbf{V}\cdot\nabla)\mathbf{V} + \nabla p = \mathbf{F} \quad \text{(in the fluid)}, \tag{1}$$

where $\mathbf{V}$ is the flow velocity, p the hydrodynamic pressure, $\mathbf{F}$ the sum of all body forces (including buoyancy and Lorentz forces). The viscosity η is assumed to be constant, while the density ρ is allowed (at least for now) to vary with temperature. Conservation of mass is enforced through the continuity equation,

$$\nabla\cdot(\rho\mathbf{V}) = 0 \quad \text{(in the fluid)}. \tag{2}$$

Equations (1) and (2) must be supplemented with a boundary condition for the fluid velocity. Denoting by $\mathbf{V}_0$ the velocity field associated with the rigid rotation of the crucible, the usual no-slip condition for viscous fluids requires that

$$\mathbf{V} = \mathbf{V}_0 \quad \text{(at the walls)}. \tag{3}$$

The balance of energy can be written as a scalar convection-diffusion equation in terms of the temperature T,

$$-\kappa\nabla^2 T + \rho c(\mathbf{V}\cdot\nabla)T = H \quad \text{(in the fluid)}, \tag{4}$$

where H is the sum of all heat sources (including dissipative and radiative heating). The thermal conductivity κ and specific heat c are assumed to be constant (in the relevant temperature range). As a boundary condition, we assume that the heat flux across the walls is proportional to the temperature difference between the fluid and the exterior of the crucible:

$$-\kappa(\nabla T)\cdot\mathbf{n} = \gamma(T - T_{\text{ext}}) \quad \text{(at the walls)}. \tag{5}$$

Here, $\mathbf{n}$ denotes the unit outward normal vector field on the surface of the fluid region; γ is the (constant) heat transfer coefficient of the walls, and T_{ext} stands for the given ambient temperature.

The electric current distribution is determined by Ohm's law,

$$\mathbf{J} = \sigma(-\nabla\phi + \mathbf{V} \times \mathbf{B}) \quad \text{(in the fluid)}, \tag{6}$$

along with the continuity equation,

$$\nabla \cdot \mathbf{J} = 0 \quad \text{(in the fluid)}, \tag{7}$$

where $\mathbf{J}$ is the electric current density, ϕ a scalar electric potential, $\mathbf{B}$ the magnetic induction, and σ the (constant) electric conductivity of the fluid. Since the exterior of the crucible is assumed to be nonconducting, the obvious boundary condition for $\mathbf{J}$ is that

$$\mathbf{J} \cdot \mathbf{n} = 0 \quad \text{(at the walls)}. \tag{8}$$

The magnetic field can be decomposed as

$$\mathbf{B} = \mathbf{B}_0 + \mathbf{B}_1,$$

where $\mathbf{B}_0$ and $\mathbf{B}_1$ represent, respectively, the applied field and the field induced by the current $\mathbf{J}$. The latter satisfies Maxwell's equations,

$$\begin{aligned} \nabla \times \mathbf{B}_1 &= \mu\mathbf{J} \quad && \text{(in the fluid)}, \\ \nabla \times \mathbf{B}_1 &= 0 \quad && \text{(in the exterior)}, \\ \nabla \cdot \mathbf{B}_1 &= 0 \quad && \text{(throughout space)}. \end{aligned} \tag{9}$$

Since the fluid is heated beyond the Curie point, μ is the magnetic permeability of free space ($4\pi \cdot 10^{-7}$ H m^{-1}). In addition, $\mathbf{B}_1$ must be continuous across the crucible walls (constant permeability, no surface currents!) and vanish at infinity (finite source!):

$$\begin{aligned} [\mathbf{B}_1] &= 0 \quad && \text{(across the walls)}, \\ \mathbf{B}_1 &= 0 \quad && \text{(at infinity)}. \end{aligned} \tag{10}$$

For any reasonably regular current distribution $\mathbf{J}$, Equations (9) and (10) admit a unique solution $\mathbf{B}_1 = \mathcal{B}(\mathbf{J})$, which is given by the Biot-Savart formula (a volume integral over the fluid region):

$$\mathcal{B}(\mathbf{J}) = -\frac{\mu}{4\pi} \int \frac{\mathbf{r} - \mathbf{s}}{|\mathbf{r} - \mathbf{s}|^3} \times \mathbf{J}(\mathbf{s})\, d^3\mathbf{s}. \tag{11}$$

The body force $\mathbf{F}$ on the right-hand side of Equation (1) includes the Lorentz force, $\mathbf{J} \times \mathbf{B}$, and the force of gravity, $\rho\mathbf{g}$, where $\mathbf{g}$ is gravitational acceleration. We employ the Boussinesq approximation to account for buoyancy forces due to temperature gradients; that is, we assume that T fluctuates in a narrow range about a reference temperature T_{ref} and that the density, in this temperature range, decreases linearly with T:

$$\frac{\rho}{\rho_{\text{ref}}} = 1 - \beta(T - T_{\text{ref}}).$$

Here, ρ_{ref} and β denote the density and thermal expansion coefficient of the fluid at the reference temperature. The force of gravity is then given by

$$\rho\mathbf{g} = \nabla p_{\text{ref}} - \beta\rho_{\text{ref}}(T - T_{\text{ref}})\mathbf{g},$$

where $\nabla p_{\text{ref}} = \rho_{\text{ref}}\,\mathbf{g}$ is the hydrostatic pressure gradient (at the reference temperature), while $\beta\rho_{\text{ref}}(T - T_{\text{ref}})\mathbf{g}$ represents the buoyancy force. Summarizing, we have

$$\mathbf{F} = \mathbf{J} \times \big(\mathbf{B}_0 + \mathcal{B}(\mathbf{J})\big) + \nabla p_{\text{ref}} - \beta\rho_{\text{ref}}(T - T_{\text{ref}})\mathbf{g}. \tag{12}$$

Following standard practice, we now introduce a reduced pressure, $p' = p - p_{\text{ref}}$, and reduced temperature, $T' = T - T_{\text{ref}}$, and replace the density ρ in Equations (1), (2), and (4) by ρ_{ref}. Also, for notational convenience, we drop the primes in p' and T' and the subscript in ρ_{ref}; that is, from now on, p, T, and ρ will denote the reduced pressure, reduced temperature, and reference density, respectively. (Note that Equations (4) and (5) remain unchanged after this reduction, except that T_{ext} must be replaced by $T_{\text{ext}} - T_{\text{ref}}$.)

The source term H in Equation (4) comprises dissipative heating due to electric currents and viscous drag as well as radiative heating due to the presence of heating elements. Thus,

$$H = \sigma^{-1}|\mathbf{J}|^2 + \frac{1}{2}\eta\,|\nabla\mathbf{V} + (\nabla\mathbf{V})^{\text{tr}}|^2 + h, \tag{13}$$

where h is a given function of position, depending on the characteristics of the heating elements. For the apparatus described in Bakhtiyarov et al. (1999), the following ansatz seems reasonable:

$$h(\mathbf{r}) = I_0\chi(\mathbf{r})\exp\big(-\alpha\, d(\mathbf{r})\big). \tag{14}$$

Here, I_0 is the output intensity of the quartz lamps, $\chi(\mathbf{r})$ an empirical function describing the intensity distribution in the light cone, α the absorption coefficient of the fluid (in the relevant frequency range, at the reference temperature), and $d(\mathbf{r})$ the penetration depth. For any reasonbly regular velocity field $\mathbf{V}$ and current distribution $\mathbf{J}$, Equations (4) and (5), with H given by (13) and (14), constitute a linear, uniformly elliptic boundary-value problem of familiar type, which has a unique solution $T = \mathcal{T}(\mathbf{V}, \mathbf{J})$. Given $\mathbf{V}$ and $\mathbf{J}$, the solution can be numerically computed in numerous ways, although no explicit representation is available.

We emphasize that both the induced magnetic field $\mathcal{B}(\mathbf{J})$ (the unique solution of the linear div-curl system (9)–(10)) and the reduced temperature $\mathcal{T}(\mathbf{V}, \mathbf{J})$ (the unique solution of the linear, elliptic boundary-value problem (4)–(5)) are easy to compute, to any desired accuracy, for any given, sufficiently regular vector fields $\mathbf{V}$ and $\mathbf{J}$. In what follows, we will therefore focus our attention on the remaining, coupled, nonlinear boundary-value problem for the velocity $\mathbf{V}$, current density $\mathbf{J}$, reduced pressure p, and electric potential ϕ, as obtained from Equations (1)–(3) (along with (12)) and (6)–(8):

$$\begin{gathered} -\eta\nabla^2\mathbf{V} + \rho(\mathbf{V} \cdot \nabla)\mathbf{V} + \nabla p = \mathbf{J} \times \big(\mathbf{B}_0 + \mathcal{B}(\mathbf{J})\big) - \beta\rho\mathcal{T}(\mathbf{V}, \mathbf{J})\mathbf{g}, \\ \sigma^{-1}\mathbf{J} + \nabla\phi = \mathbf{V} \times \big(\mathbf{B}_0 + \mathcal{B}(\mathbf{J})\big), \\ \nabla \cdot \mathbf{V} = 0 \quad \text{and} \quad \nabla \cdot \mathbf{J} = 0 \quad \text{(in the fluid)}, \\ \mathbf{V} = \mathbf{V}_0 \quad \text{and} \quad \mathbf{J} \cdot \mathbf{n} = 0 \quad \text{(at the walls)}. \end{gathered} \tag{15}$$

Note that the above, due to the presence of the operators $\mathcal{B}$ and $\mathcal{T}$, is in fact a system of integro-differential equations ($\mathcal{B}$ is a

linear, first-order integral operator, $\mathcal{T}$ a nonlinear, second-order integral operator). As a consequence, some care must be exercised in choosing linearization/iteration schemes for the numerical solution of the discretized equations, in order to avoid the occurrence of dense matrices (see the following section).

A careful order-of-magnitude analysis was performed to assess the relative importance of the various terms in the equations. The conclusions, as pertaining to the laboratory conditions described in Bakhtiyarov et al. (1999), can be summarized as follows (details will be presented elsewhere):

(a) Lorentz forces and inertial forces are of comparable magnitude; both are large compared to buoyancy and viscous forces, which are roughly comparable.

(b) The induced magnetic field is small compared to the applied field (but less so for high angular velocities).

(c) Convective heat transfer dominates diffusion (but less so for small angular velocities). Viscous heating is small compared to Joule heating; both are negligible compared to diffusion and convection.

It is therefore feasible to neglect Joule and viscous heating when computing the temperature distribution. Neglecting temperature fluctuations altogether, that is, setting $\mathcal{T}(\mathbf{V},\mathbf{J}) = 0$, is viable only as a first approximation. The same can be said with regard to the induced magnetic field $\mathcal{B}(\mathbf{J})$.

2. FINITE-ELEMENT DISCRETIZATION

The numerical solution of the boundary-value problem (15) is based on a mixed variational formulation in the spirit of the well-known Babuska-Brezzi theory; see, for example, Brezzi and Fortin (1991). This formulation is obtained by multiplying the four PDEs by suitable test functions $\mathbf{W}$ (for the velocity), $\mathbf{K}$ (for the current density), q (for the pressure), and ψ (for the electric potential) and integrating the equations over the fluid region. The two identities resulting from the momentum balance and Ohm's law are added together, and so are the identities resulting from the two continuity equations. After some algebra and several integrations by parts (using the boundary conditions), one arrives at two equations of the form

$$\begin{aligned} a_0\big((\mathbf{V},\mathbf{J}),(\mathbf{W},\mathbf{K})\big) + a_1\big((\mathbf{V},\mathbf{J}),(\mathbf{V},\mathbf{J}),(\mathbf{W},\mathbf{K})\big) \\ + b\big((\mathbf{W},\mathbf{K}),(p,\phi)\big) = f\big((\mathbf{V},\mathbf{J}),(\mathbf{W},\mathbf{K})\big), \end{aligned} \tag{16}$$

$$b\big((\mathbf{V},\mathbf{J}),(q,\psi)\big) = 0, \tag{17}$$

where a_0 (a bilinear form), a_1 (a trilinear form), and b (a bilinear form) are given by

$$\begin{aligned} &a_0\big((\mathbf{W}_1,\mathbf{K}_1),(\mathbf{W}_2,\mathbf{K}_2)\big) \\ &\quad = \eta\int(\nabla\mathbf{W}_1)\cdot(\nabla\mathbf{W}_2) + \sigma^{-1}\int\mathbf{K}_1\cdot\mathbf{K}_2 \\ &\qquad + \int\big((\mathbf{K}_2\times\mathbf{B}_0)\cdot\mathbf{W}_1 - (\mathbf{K}_1\times\mathbf{B}_0)\cdot\mathbf{W}_2\big), \\ &a_1\big((\mathbf{W}_1,\mathbf{K}_1),(\mathbf{W}_2,\mathbf{K}_2),(\mathbf{W}_3,\mathbf{K}_3)\big) \\ &\quad = \frac{\rho}{2}\int\Big(\big((\mathbf{W}_1\cdot\nabla)\mathbf{W}_2\big)\cdot\mathbf{W}_3 - \big((\mathbf{W}_1\cdot\nabla)\mathbf{W}_3\big)\cdot\mathbf{W}_2\Big) \\ &\qquad + \int\Big(\big(\mathbf{K}_3\times\mathcal{B}(\mathbf{K}_1)\big)\cdot\mathbf{W}_2 - \big(\mathbf{K}_2\times\mathcal{B}(\mathbf{K}_1)\big)\cdot\mathbf{W}_3\Big), \end{aligned}$$

and

$$b\big((\mathbf{W},\mathbf{K}),(q,\psi)\big) = -\int(\nabla\cdot\mathbf{W})\,q + \int\mathbf{K}\cdot(\nabla\psi),$$

while f (a nonlinear forcing term) is given by

$$f\big((\mathbf{W}_1,\mathbf{K}_1),(\mathbf{W}_2,\mathbf{K}_2)\big) = -\beta\rho\int\mathcal{T}(\mathbf{W}_1,\mathbf{K}_1)\,\mathbf{g}\cdot\mathbf{W}_2.$$

Under mild assumptions on the data, solving the original boundary-value problem (15) is equivalent to finding vector fields $\mathbf{V}$ and $\mathbf{J}$ and scalar fields p and ϕ such that (a) $\mathbf{V} = \mathbf{V}_0$ on the boundary of the fluid region and (b) Equations (16) and (17) are satisfied for all relevant test functions $\mathbf{W}$, $\mathbf{K}$, q, and ψ. The essential boundary condition for $\mathbf{V}$ must be enforced separately, and as a consequence, the velocity test functions must vanish on the boundary. The boundary condition for $\mathbf{J}$ is a natural one and can be recovered from Equation (17).

A finite-element discretization of the problem is obtained by requiring that Equations (16) and (17) be satisfied for only a finite number of test functions, namely, the basis functions of suitably chosen finite-element spaces. Also, the boundary condition for $\mathbf{V}$ must be approximately satisfied in an appropriate sense, for example, by requiring that $\mathbf{V} = \mathbf{V}_0$ at the boundary nodes of the finite-element grid (assuming the use of Lagrangian elements). This leads to a finite-dimensional system of nonlinear, algebraic equations that can be solved by way of linearization and iteration.

Equation (16) is linearized by replacing the first arguments of the forms a_1 and f by initial guesses or previously computed values $\mathbf{V}_{\text{old}}$ and $\mathbf{J}_{\text{old}}$ for the velocity field and current density. In terms of the original PDEs, this amounts to lagging the first velocity in the inertia term $(\mathbf{V}\cdot\nabla)\mathbf{V}$, the induced magnetic field $\mathcal{B}(\mathbf{J})$, and the temperature distribution $\mathcal{T}(\mathbf{V},\mathbf{J})$. Lagging the magnetic field and temperature also prevents the occurrence of dense matrices despite the presence of the integral operators $\mathcal{B}$ and $\mathcal{T}$. Given an initial guess or previously computed pair $(\mathbf{V}_{\text{old}},\mathbf{J}_{\text{old}})$, the linearized equations are solved to update $(\mathbf{V},\mathbf{J})$ and to compute (p,ϕ). This process is iterated until the change in $(\mathbf{V},\mathbf{J})$, as measured in a suitable norm, drops below a given tolerance. At the beginning of each iteration, the induced magnetic field $\mathcal{B}(\mathbf{J}_{\text{old}})$ and the temperature distribution $\mathcal{T}(\mathbf{V}_{\text{old}},\mathbf{J}_{\text{old}})$ are computed by evaluating the Biot-Savart integral (11) and by solving the linear, elliptic boundary-value problem (4)–(5), with H given by (13) and (14). A simplified flow diagram is shown in Figure 1.

In order to guarantee stability and convergence of the algorithm, some care must be exercised in choosing finite-element spaces. The main restriction is that the elements used to approximate velocity and pressure as well as those used for electric current density and potential must satisfy so-called inf-sup conditions or LBB (Ladyzhenskaya-Babuska-Brezzi) conditions. In the present implementation of the method, we construct a Lipschitz-continuous coordinate transformation that maps the physical domain (a circular cylinder) onto a circumscribed square cylinder (the computational domain), allowing all computations to be performed on a logically rectangular grid. The square cylinder is decomposed into rectangular parallelepipeds of equal

size. This allows us to use standard Taylor-Hood elements for velocity and pressure, namely, continuous piecewise triquadratics for the velocity and continuous piecewise trilinears for the pressure. These elements are known to satisfy the LBB condition. It is natural to use continuous piecewise triquadratics for the electric potential as well, but the LBB condition then requires a somewhat nonstandard finite-element space for the current density: this space must contain the gradients of continuous piecewise triquadratics. Thus, the elements used to approximate the ith component of the current density are piecewise linear and generally discontinuous in the ith variable, but continuous and piecewise quadratic in the remaining two variables.

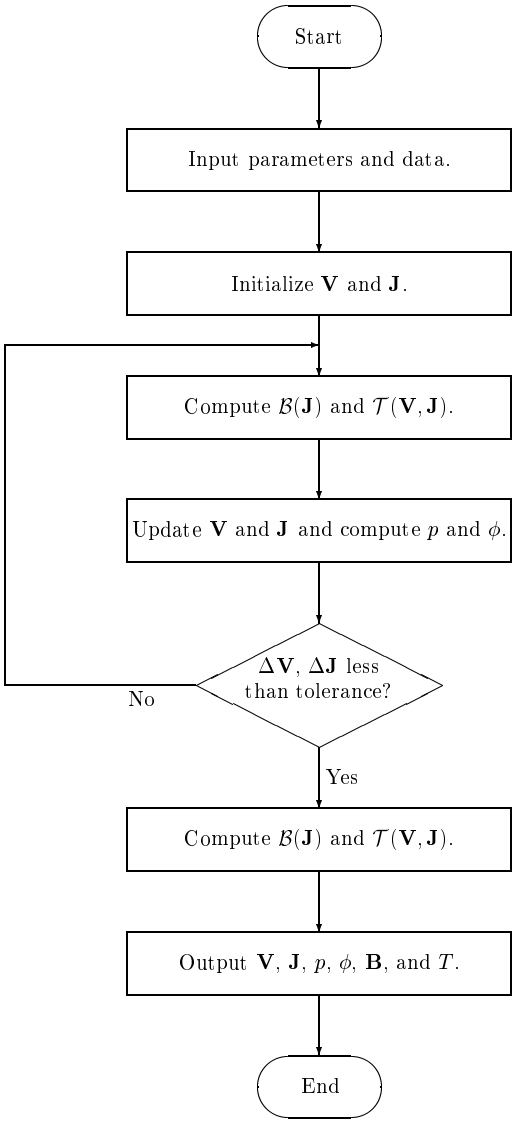

Figure 1. Simplified flow diagram for the iterative solution of the discretized problem.

Basis functions for the above finite-element spaces are constructed using standard 27-node Lagrange elements for the velocity and potential, standard 8-node Lagrange elements for the pressure. For the ith component of the current density, we use Hermite elements with nine nodes, namely, those nodes of the standard 27-node Lagrange element that are not on faces perpendicular to the ith coordinate axis; two degrees of freedom are associated with each of these nodes, namely, the value of the function and the value of its derivative with respect to the ith variable. (Instead of 9-node Hermite elements, we could of course use 18-node Lagrange elements, but we would then be unable to utilize the same nodes as for velocity, pressure, and potential.)

Since pressure and potential can be determined only up to additive constants, both are set equal to zero at one node of the finite-element grid. The essential boundary condition for the velocity field is enforced by setting $\mathbf{V} = \mathbf{V}_0$ at all boundary nodes.

With these choices, and in light of general results of finite-element theory, the discretization error is expected to decrease quadratically with the grid size. For further details, including rigorous error estimates and a numerical validation of the predicted quadratic rate of convergence, we refer to Meir and Schmidt (1999b).

3. NUMERICAL EXPERIMENTS AND DISCUSSION

The method described in the previous section was implemented and tested in a series of computer experiments. Although these experiments are of a preliminary nature, they demonstrate the feasibility of the approach.

While the present implementation allows the computation of the induced magnetic field $\mathcal{B}(\mathbf{J})$, via evaluation of the Biot-Savart integral (11), it does not yet incorporate the effect of temperature fluctuations; that is, $\mathcal{T}(\mathbf{V}, \mathbf{J})$ is assumed to be zero. According to the remarks at the end of Section 1, this is viable only as a first approximation. Adding a subroutine for the computation of $\mathcal{T}(\mathbf{V}, \mathbf{J})$ poses no problem in principle, but requires laboratory experiments to validate the proposed model (14) for the radiative heat source (including measurements of the intensity distribution in the light cone and infrared absorption properties of the metal samples).

Besides neglecting temperature fluctuations, the computations have thus far been limited to the laminar flow regime with small angular velocities and modest magnetic fields. All computations were done on a workstation, which, in conjunction with the sheer size of this fully three-dimensional problem, precluded the use of all but very coarse finite-element grids. The simulation of more realistic flow conditions would require much higher spatial resolution (that is, much finer grids) and ultimately, the incorporation of a turbulence model.

We used the discretization and iteration scheme described in Section 2 on a grid of 432 elements with a total of 4,225 nodes. The ensuing sparse linear systems, with roughly 30,000 unknowns (not counting the induced magnetic field), were solved directly, using a standard linear-algebra package. Stiffness matrices and load vectors were computed with a high-order Gaus-

sian quadrature rule on the reference element. When desired, the induced magnetic field could be determined by evaluating the Biot-Savart integral via Gaussian quadrature.

Given below are the results of a simulation of one of the experiments described in Bakhtiyarov et al. (1999), where a cylindrical column of liquid aluminum is steadily rotated in a uniform magnetic field perpendicular to the cylinder axis; see Figure 2 for the geometry of the configuration and the table below for the data and parameters used (MKS units are employed throughout).

Table 1. Data and parameters for computer experiment.

R	cylinder radius	$1.27 \cdot 10^{-2}$ m
L	cylinder height	$10.16 \cdot 10^{-2}$ m
ω	angular frequency	1.05 s^{-1} (10 rpm)
B_0	applied field	0.1 T
ρ	density	$2.38 \cdot 10^{3}$ kg m^{-3}
η	viscosity	$1.8 \cdot 10^{-3}$ kg m^{-1} s^{-1}
σ	electric conductivity	$4.1 \cdot 10^{6}$ mho m^{-1}
μ	magnetic permeability	$1.26 \cdot 10^{-6}$ H m^{-1}

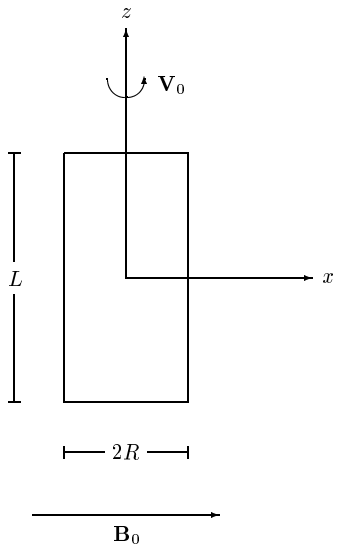

Figure 2. Geometry of the configuration. (Not to scale. Aspect ratio L/2R is 4.)

Figures 4–7 show the computed current, potential, velocity, and pressure distributions. Clearly visible is a closed current loop parallel to the plane $y = 0$ (which contains both the axis of the magnetic field and the axis of rotation). Significant potential gradients arise only near the top and bottom of the column. The velocity field is almost purely horizontal, the pressure almost purely radial. Figure 8, depicting the flow pattern in the plane $z = 0$, reveals significant counter-rotation associated with two kidney-shaped vortices, centered on the x-axis (the axis of the magnetic field) and equidistant from the center. The same general pattern is found in horizontal cross-sections along much of the cylinder axis. Due to the no-slip boundary condition, a transition to rigid rotation occurs near the top and bottom, but the transition layers are fairly thin (compare Figures 8 and 9). More quantitative information can be inferred from azimuthal velocity profiles, parallel and perpendicular to the magnetic field. Figure 10 shows the y-velocity along the x-axis, Figure 11 the negative of the x-velocity along the y-axis, both in the plane $z = 0$. Figures 12 and 13 give essentially the same information, but with respect to the rest frame of the cylinder; that is, they show the azimuthal components of the *induced* velocity $\mathbf{V} - \mathbf{V}_0$ (where $\mathbf{V}_0$ is the velocity field associated with a rigid rotation at constant angular frequency ω). The induced velocity is generally antiparallel to $\mathbf{V}_0$ and of the same order of magnitude. As a consequence, the fluid is virtually at rest in the region between the two vortices seen in Figures 8 and 9. Figures 14 and 15 support the observation that the induced velocity does not appreciably decrease along much of the cylinder axis. (It must, of course, go to zero in the transition layers at the top and bottom.)

In this simulation, the induced magnetic field $\mathcal{B}(\mathbf{J})$ was fully accounted for. We then repeated the experiment, this time neglecting $\mathcal{B}(\mathbf{J})$. As expected (in view of a magnetic Reynolds number of order 10^{-3}), we found the difference to be insignificant.

The results of the simulation are easily explained, at least qualitatively, by inspection of the leading-order terms in the Navier-Stokes equations and Ohm's law. The velocity field associated with the rigid rotation of the cylinder is $\mathbf{V}_0 = \omega(-y\mathbf{i}+x\mathbf{j})$. This is a solution of the Navier-Stokes equations with zero body forces. No viscous shear is associated with $\mathbf{V}_0$, and inertia is balanced by a radial pressure gradient: $\rho(\mathbf{V}_0 \cdot \nabla)\mathbf{V}_0 = -\nabla p_0$ with $p_0 = \frac{1}{2}\rho\omega^2(x^2 + y^2)$. Due to the presence of the applied magnetic field $\mathbf{B}_0 = B_0\mathbf{i}$, a current $\mathbf{J}_0 = \sigma\mathbf{V}_0 \times \mathbf{B}_0 = -\sigma\omega B_0 x\mathbf{k}$ is induced. This current is parallel to the z-axis and concentrated in two near-wall regions centered on the x-axis (see Figure 3); it is not accompanied by a potential gradient (since $\mathbf{V}_0 \times \mathbf{B}_0$ is solenoidal). The finite length of the cylinder forces return currents to flow parallel to the x-axis in boundary layers near the top and bottom of the cylinder; those are associated with potential gradients.

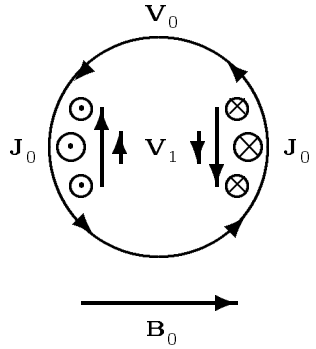

Figure 3. Induced current and flow field.

The current $\mathbf{J}_0$ and applied field $\mathbf{B}_0$ generate a Lorentz force $\mathbf{J}_0 \times \mathbf{B}_0 = -\sigma\omega B_0^2 x\mathbf{j}$. This force is rotational and cannot be balanced by a pressure gradient; it thus accelerates the fluid, resulting in a secondary velocity $\mathbf{V}_1$, antiparallel to $\mathbf{V}_0$ (see Figure 3). This explains the general flow pattern (and in particular, the kidney-shaped vortices) seen in Figures 8 and 9. According to the remarks at the end of Section 1, it must be the inertial force, $\rho(\mathbf{V}_1 \cdot \nabla)\mathbf{V}_1$, which balances $\mathbf{J}_0 \times \mathbf{B}_0$. A characteristic value of $\mathbf{V}_1$ is thus given by $V_1 = (\sigma\omega/\rho)^{1/2} R B_0$, and the ratio $V_1/V_0 = (\sigma/\rho\omega)^{1/2} B_0$ is roughly of order one. (This scaling argument applies as long as the hydrodynamic Reynolds number is large compared to unity. This is the case even for fairly small ω, but of course not in the limit $\omega \to 0$.)

One conclusion is that applying a relatively strong magnetic field at modest speeds of rotation can result in significant counter-rotation of the melt in the two near-wall regions, centered on the axis of the magnetic field, where the current $\mathbf{J}_0$ is concentrated. Since the rotation of the cylinder constantly transports fluid particles through these regions, this may be an efficient stirring mechanism.

CONCLUSIONS

A new aproach to the mathematical modeling and computational simulation of fully three-dimensional, electromagnetically and thermally driven liquid-metal flow was developed and applied to simulate the flow of a metallic melt in a cylindrical crucible, rotating steadily in a uniform magnetic field perpendicular to the cylinder axis. A finite-element based discretization and iteration scheme was designed for the numerical solution of the underlying nonlinear PDEs. The results of preliminary computer experiments (limited to the laminar flow regime and not accounting for temperature fluctuations) were shown to agree with theoretical predictions. It was found that already modest magnetic fields and angular velocities can lead to significant counter-rotation and efficient stirring of the melt.

ACKNOWLEDGEMENT

The work of Meir and Schmidt was supported by the National Science Foundation under Grant DMS-9625096.

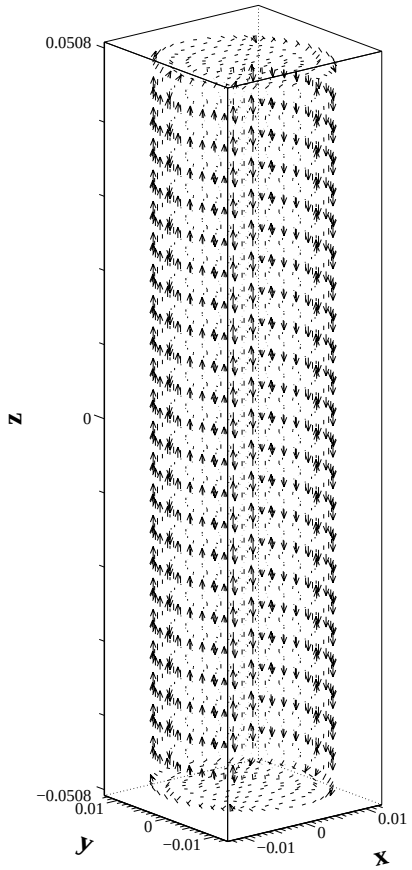

Figure 4. Current density.

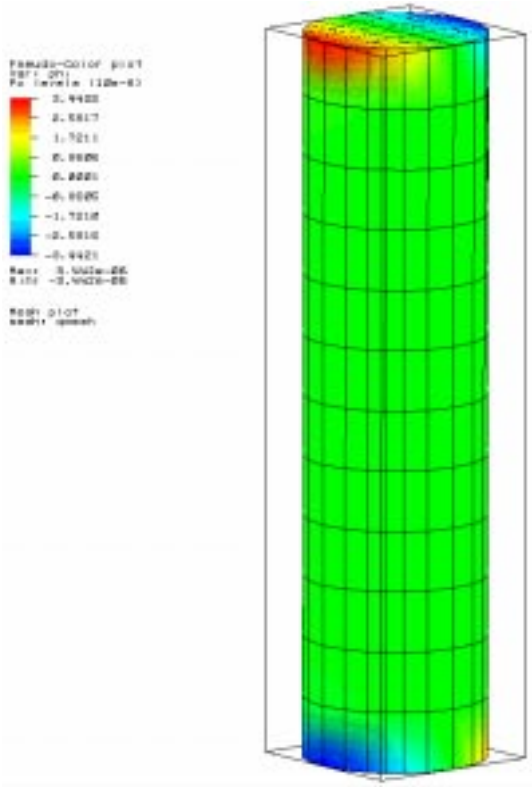

Figure 5. Electric potential.

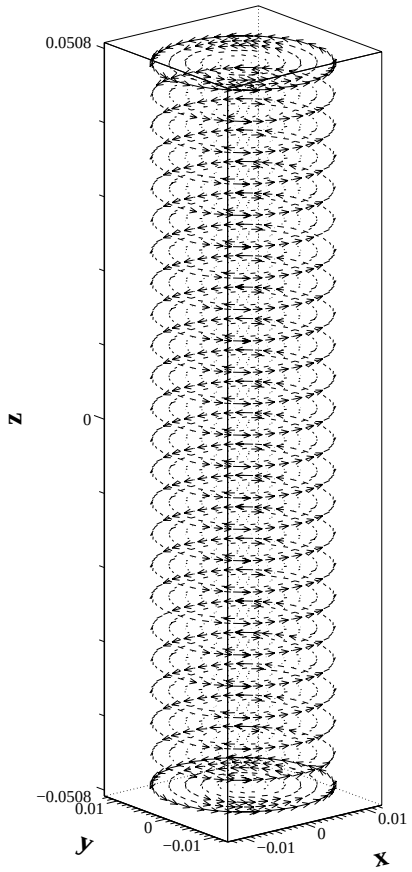

Figure 6. Velocity field.

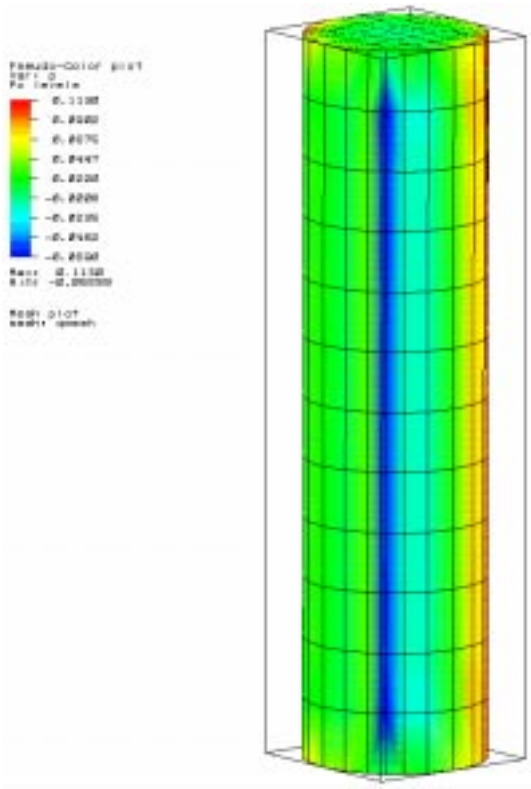

Figure 7. Pressure distribution.

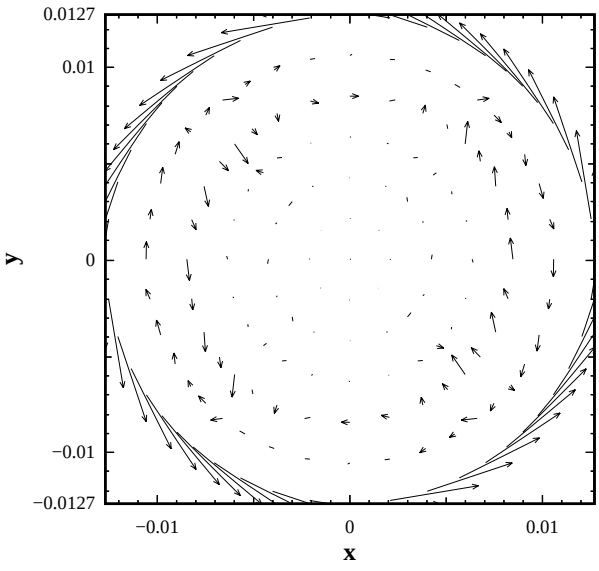

Figure 8. Flow pattern in the plane z=0.

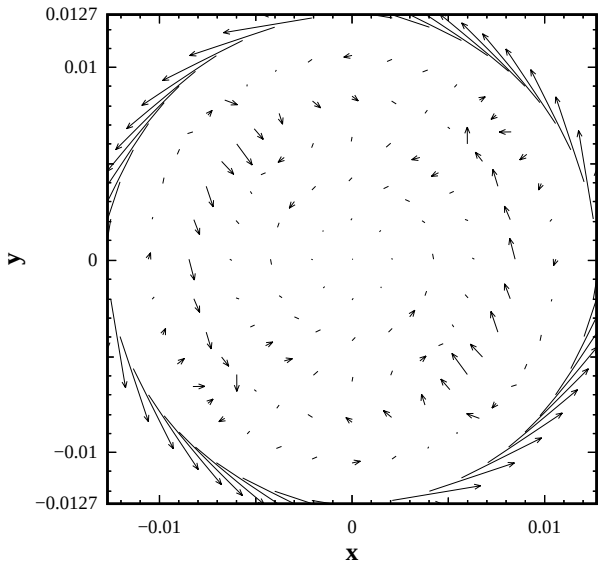

Figure 9. Flow pattern in the plane z=5L/12.

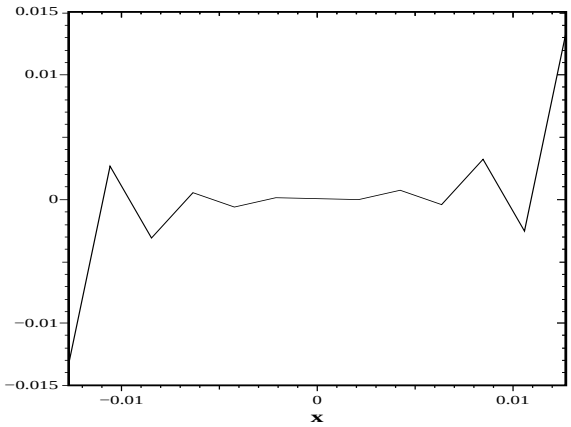

Figure 10. Azimuthal velocity in the plane z=0, along the x-axis (parallel to the magnetic field).

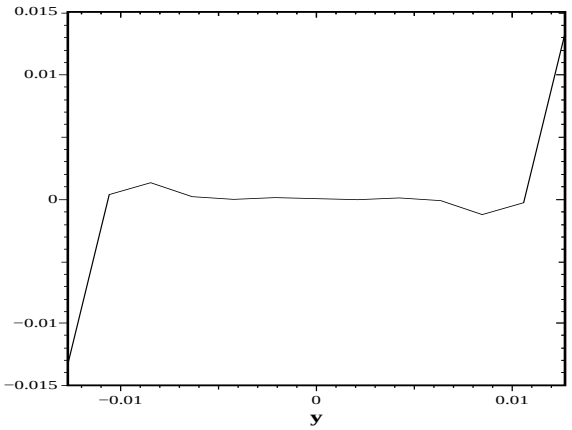

Figure 11. Azimuthal velocity in the plane z=0, along the y-axis (perpendicular to the magnetic field).

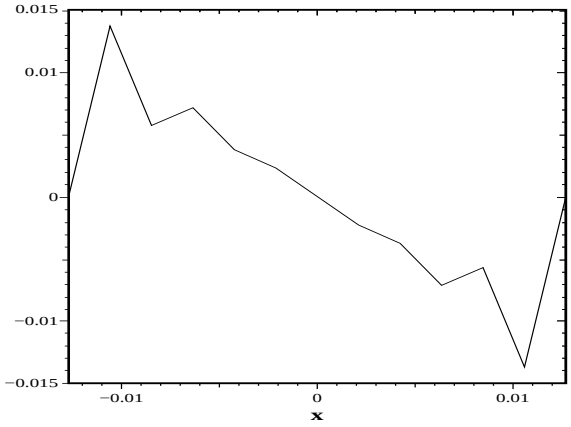

Figure 12. Induced azimuthal velocity (V-V_0) in the plane z=0, along the x-axis.

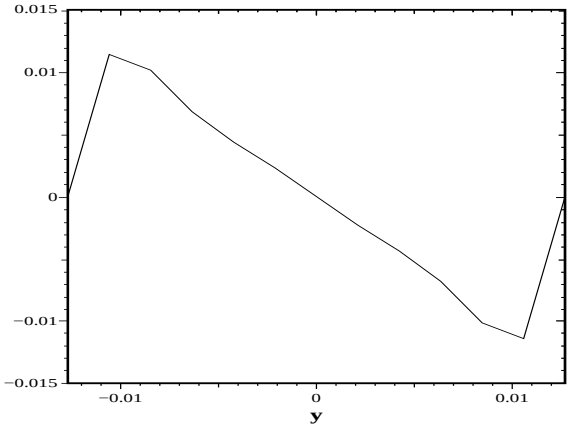

Figure 13. Induced azimuthal velocity (V-V_0) in the plane z=0, along the y-axis.

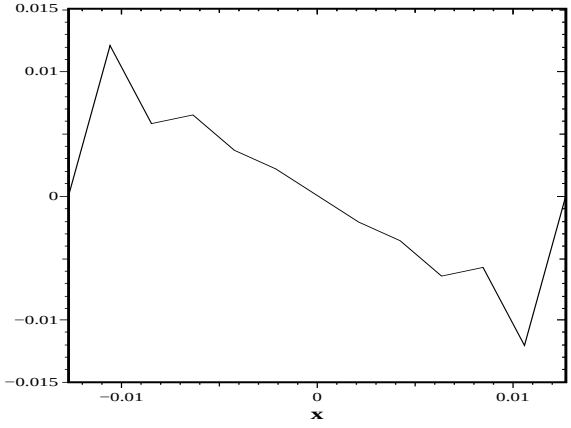

Figure 14. Induced azimuthal velocity (V-V_0) in the plane z=5L/12, along the x-axis.

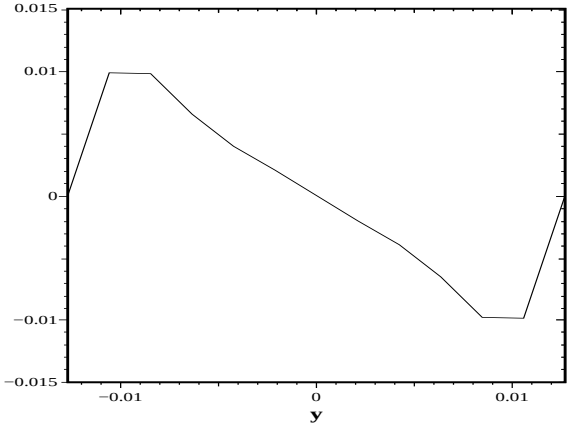

Figure 15. Induced azimuthal velocity (V-V_0) in the plane z=5L/12, along the y-axis.

REFERENCES

Bakhtiyarov, S.I., Overfelt, R.A., Meir, A.J., and Schmidt, P.G., 1999, "Velocity, Potential, and Temperature Distributions in Molten Metals During Electromagnetic Stirring. Part I: Experimental Measurements" (in these proceedings).

Brezzi, F., and Fortin, M., 1991, *Mixed and Hybrid Finite Element Methods*, Springer, New York.

Cho, Y.W., Chung, S.H., Shim, J.D., Dement'ev, S., and Ivanov, S., 1999, "Fluid Flow and Heat Transfer in Molten Metal Stirred by a Circular Inductor," *International Journal of Heat and Mass Transfer*, Vol. 42, pp. 1317–1326.

Davidson, P.A., and Hunt, J.C.R., 1987, "Swirling Recirculating Flow in a Liquid-metal Column Generated by a Rotating Magnetic Field," *Journal of Fluid Mechanics*, Vol. 185, pp. 67–106.

Hughes, W.F., and Young, F.J., 1966, *The Electromagnetodynamics of Fluids*, Wiley, New York.

Meir, A.J., and Schmidt, P.G., 1998, "Analysis and Finite Element Simulation of MHD Flows, with an Application to Seawater Drag Reduction," in: Proceedings, International Symposium on Seawater Drag Reduction, J.C.S. Meng, ed., Naval Undersea Warfare Center, Newport, Rhode Island, pp. 401–406.

Meir, A.J., and Schmidt, P.G., 1999a, "Analysis and Finite Element Simulation of MHD Flows, with an Application to Liquid Metal Processing," in: *Fluid Flow Phenomena in Metals Processing*, Proceedings, 1999 TMS Annual Meeting, N. El-Kaddah et al., eds., Minerals, Metals & Materials Society, Warrendale, Pennsylvania, pp. 561–569.

Meir, A.J., and Schmidt, P.G., 1999b, "Analysis and Numerical Approximation of a Stationary MHD Flow Problem with Nonideal Boundary," *SIAM Journal on Numerical Analysis*, Vol. 36, pp. 1304–1332.

Meyer, J.-L., Durand, F., Ricou, R., and Vivès, C., 1984, "Steady Flow of Liquid Aluminum in a Rectangular-Vertical Ingot Mold, Thermally or Electromagnetically Activated," *Metallurgical Transactions B*, Vol. 15, pp. 471–478.

Moffatt, H.K., 1965, "On Fluid Flow Induced by a Rotating Magnetic Field," *Journal of Fluid Mechanics*, Vol. 22, pp. 521–528.

Prescott, P.J., and Incropera, F.P., 1993, "Magnetically Damped Convection During Solidification of a Binary Metal Alloy," *ASME Journal of Heat Transfer*, Vol. 115, pp. 302–310.

Saluja, N., Ilegbusi, O.J., and Szekely, J., 1990, "On the Calculation of the Electromagnetic Force Field in the Circular Stirring of Metallic Melts," *Journal of Applied Physics*, Vol. 68, pp. 5845–5850.

Spitzer, K.-H., Dubke, M., and Schwerdtfeger, K., 1986, "Rotational Electromagnetic Stirring in Continuous Casting of Round Strands," *Metallurgical Transactions B*, Vol. 17, pp. 119–131.

Vivès, Ch., and Ricou, R., 1985, "Fluid Flow Phenomena in a Single Phase Coreless Induction Furnace," *Metallurgical Transactions B*, Vol. 16, pp. 227–235.